Research Square

Preprints are preliminary reports that have not undergone peer review.
They should not be considered conclusive, used to inform clinical practice,
or referenced by the media as validated information.

The Norma arm: star formation in a bar-driven shock front in the Milky Way

Hillary Davis

hdav7324@uni.sydney.edu.au

University of Sydney https://orcid.org/0009-0006-2670-0453

Joss Bland-Hawthorn

University of Sydney

Thor Tepper-Garcia

University of Sydney

Oscar Agertz

Lund Observatory, Division of Astrophysics, Department of Physics

Article

Keywords:

Posted Date: February 25th, 2026

DOI: https://doi.org/10.21203/rs.3.rs-8876034/v1

License: This work is licensed under a Creative Commons Attribution 4.0 International License.
Read Full License

Additional Declarations: There is **NO** Competing Interest.

The Norma arm: star formation in a bar-driven shock front in the Milky Way

Hillary Davis[1*], Joss Bland-Hawthorn[1], Thor Tepper-García[1], Oscar Agertz[2]

[1*]Sydney Institute for Astronomy, School of Physics, University of Sydney, NSW 2006, Australia.
[2]Lund Observatory, Division of Astrophysics, Department of Physics, Lund University, Box 118, SE-22100 Lund, Sweden.

*Corresponding author(s). E-mail(s): hdav7324@uni.sydney.edu.au;

Abstract

Masers associated with young high-mass stars have been used to trace a segment of the "Norma arm" extending from one end of the Galaxy's central stellar bar (Quadrant I). Recent work suggests that these masers may reside along a spiral arm or occupy the dominant $\boldsymbol{x_1}$ stellar orbits that give the bar its shape. We now argue for a very different interpretation using a new generation of N-body, hydrodynamic simulations. We believe the million-year old masers instead trace a feature of the bar's dynamics, specifically, a shock front induced by the bar's torque on the surrounding gas. The bar-driven shock front is also delineated by dust, revealing that this feature is a site of ongoing star formation. This insight brings new light on our understanding of star formation processes in the Milky Way. By associating the dust lane and masers with the simulated shock front, we determine the bar's parameters to be: $\boldsymbol{a_{\rm bar} \approx 4.3}$ kpc, $\boldsymbol{b_{\rm bar} \approx 2.3}$ kpc and $\boldsymbol{20^\circ \lesssim \phi \lesssim 25^\circ}$, where $\boldsymbol{a}$ and $\boldsymbol{b}$ are the bar's semi-major and semi-minor half-lengths, and $\boldsymbol{\phi}$ its inclination angle.

Keywords: keyword1, Keyword2, Keyword3, Keyword4

Maser observations from the BeSSeL Survey and Japanese VERA project have previously been used to trace the "Norma arm" from its origin near the Galactic bar end, at $(X, Y) \approx (3, 2)$ kpc, curving anticlockwise to $(X, Y) \approx (2, 5)$ kpc [1]. In some interpretations, the Norma arm continues around to the far side of the Galactic centre, connecting with the Outer arm – the so-called "Norma-Outer arm" [1]. However, recent work suggests that some of the young stars traditionally attributed to Norma actually reside on x_1 orbits of the Galactic bar, in which case the arm terminates at the bar's end [2]. The number of spiral tracers identified along Norma remains limited due to its greater distance from the Sun compared to the well-established major spiral arms (e.g. Perseus, Sagittarius-Carina, Scutum-Centaurus), leaving this arm less well-studied [3].

The Milky Way's stellar bar leaves a distinct imprint on the corresponding gas distribution. Within the central few kiloparsecs, there are a few key structures in the gas, including: (i) a nuclear disc/ring or Central Molecular Zone (CMZ), which is a dense ring of molecular gas [4, 5, 6, 7, 8]; (ii) two distinct dust lanes, which we argue follow bar-generated shock fronts along the outer edges of the bar. These features of the MW's gas distribution are seen in stellar bars of external galaxies: e.g. NGC 1433 observed with the James Webb Space telescope (available at https://science.nasa.gov/asset/webb/ngc-1433-miri-image).

Gas structures in the bar region are commonly understood with reference to x_1 and x_2 orbits. Gas flows inward along the x_1 orbit family, eventually reaching an innermost 'cusped' x_1 orbit, within which x_1 orbits become self-intersecting (with loops at each end) [9, 10, 6, 11]. At smaller, inner radii, x_2 orbits appear – oval shaped orbits whose semi-major axes are oriented perpendicular to the bar, in contrast to x_1 orbits that are oriented parallel to the bar. The pericentre of the cusped x_1 orbit grazes the apocentre of the outermost x_2 orbits, which causes shocks to occur [9, 6, 11, 12, 6, 13]. Accurately identifying the location of bar dust lanes or shock fronts would allow us to constrain key parameters, e.g. bar size, orientation angle, and the bar's influence.

In the local universe, star formation (SF) is often suppressed in stellar bars compared to spiral arms further out in the disc [14, 12, 15, 16, 17, 18, 19, 13]. Here, we define the bar region as the area between the nuclear disc and the bar ends. Star formation is commonly enhanced at the bar ends and within the nuclear disc [20, 21, 22, 23, 24], but low along the dust lanes, despite their substantial reservoirs of dense gas. This suppression of SF in the bar region is particularly true for straight dust lanes, which are characteristic of stronger bars with more significant shear. However, it is not universal: some local bars exhibit significant SF along their length. In particular, curved dust lanes, often associated with weaker bars, are more likely to host some SF [25]. The suppression of star formation in bar regions has been linked to several mechanisms, including bar torques that funnel gas inward, depleting the bar region of fuel for star formation [26, 27, 28, 29], or bar-driven shocks and shear, which increase turbulence and stabilize the gas against gravitational collapse [15, 30, 31, 13].

Furthermore, the Galactic bar's properties are still uncertain and require better constraints. There is an ongoing debate about whether the bar is long and slow ($R_\mathrm{b} \approx 5$ kpc and pattern speed $\Omega_\mathrm{p} \approx 35 - 45$ km s^{-1} kpc^{-1}) [32, 33, 34, 35] or short and fast ($R_\mathrm{b} \approx 3.5$ kpc and $\Omega_\mathrm{p} \approx 50 - 60$ km s^{-1} kpc^{-1}) [36, 37, 38, 39, 40, 41]. The observed

$(\ell, V_{\rm los})$ − Galactic longitude and line-of-sight velocity − distributions of HI and CO gas in the Milky Way have been widely used in attempts to improve estimates the Galactic bar's properties [9, 42, 43, 44, 4, 45, 46, 47, 48].

In this work, we argue that masers, typically linked to regions of massive star formation, align with the Galactic bar's dust lane in Quadrant I. This association arises from matching the "Norma" masers with the bar shock front in our simulations. In this way: (i) we identify a *curved* dust lane, supporting an argument for a weaker bar [25]; (ii) we find that star formation is not fully suppressed in the bar region of the Milky Way, potentially because curved dust lanes are associated with weaker bar shear and shock; (iii) we argue that the Norma arm is not a spiral arm, but a shock front along the Galactic bar; (iv) we are able to fully constrain the bar's dimensions. There are many different definitions of bar length in the pre-existing literature [49]. In this work, we define the size of the Galactic bar as the extent of the bar-supporting cusped x_1 orbit (see [12], Fig. 10 for a diagram and Section 6 for further details). Hence, we estimate the bar dimensions to be: $a_{\rm bar} \approx 4.3$ kpc and $b_{\rm bar} \approx 2.3$ kpc; (iv) we are able to constrain the bar's inclination angle to $\phi \approx 20^\circ - 25^\circ$.

1 Kinematic Error maps

The kinematic distance (KD) method estimates the distance of a gas cloud from the Sun using its Galactic longitude (ℓ) and line-of-sight velocity ($V_{\rm los}$), and by assuming circular motion. To evaluate the accuracy of this approach, we apply the KD method to an N-body hydrodynamical simulation of a Milky Way–like galaxy (see Section 8 for details).

In Fig. 1 (bottom row, left panel), we introduce a basic map of kinematic distance error, $(d_{\rm k} - d_{\rm true})/d_{\rm true}$, for our model at $t = 3.95$ Gyr. Here $d_{\rm k}$ is the kinematic distance estimate, while $d_{\rm true}$ is the actual heliocentric distance taken from the simulation. To put these results in context, the first row of Fig. 1 displays a stellar density projection (left) and gas density projection (right) for our simulation at the same time. The model features a stellar bar, which we have oriented at a 25° angle relative to the $x = 0$ axis, marked by the black dashed lines, or equivalently the cyan dashed lines overlaying the gas density projection.

There are several key features about the KD error map of Fig. 1 that we want to emphasise:

- There are alternating regions of positive (red) and negative (blue) errors, which are often separated by zones of low error (white). This reflects transitions between overestimated and underestimated distances. These transitions are particularly pronounced near the spiral arms and bar.
- KD estimates are high near $\ell = 0^\circ$. This is because the denominator of Equation 1 becomes poorly constrained with $\sin\ell \to 0$ and $V_{\rm los} \to 0$. Consequently, regions with $\ell \lesssim 30^\circ$ are commonly excluded from KD-based analyses in both observational and simulation-based studies [50, 51, 52]. Additionally, the white patches near $\ell = 0^\circ$ in the KD error maps of Fig. 1 correspond to points omitted from our analysis because they have $V_{\rm los} <= -\Theta_0 \sin\ell$, which yields negative (unphysical) estimates for R.

As a brief note, we use several cuts when applying the KD method to the simulation. We exclude some low-mass, high velocity gas parcels (mass < 50 $M_\odot$ or $|V_{\rm los}| > 300$ km/s), which are occasionally generated from stellar feedback in the model. These produce unphysical KD estimates otherwise. The square-shaped features visible in the KD map of Fig. 1 result from smoothing over the remaining gas after these cuts.

- High KD errors occur near the Sun. Analytically, $\frac{\partial R}{\partial V_{\rm los}} \propto \frac{1}{(\Theta_0 \sin \ell + V_{\rm los})^2}$. Near the Sun $V_{\rm los} \approx 0$, while at larger radii $V_{\rm los}$ tends to vary between -300 and +300. This means that small variations in $V_{\rm los}$ lead to large changes in estimated R close to the Sun; meanwhile at large heliocentric distances, small variations in $V_{\rm los}$ changes R estimates less.
- Importantly, the *tangent-point (TP) circle – the circle of sub-central points between* $(-8.5, 0)$ *and the Galactic centre where terminal velocities occur in the case of pure circular motion – leaves a distinct imprint on the KD error map.* There are sharp transitions in KD error across the TP circle, often due to switching between positive and negative $d_{\rm k}$ solutions, corresponding to the the $\pm\sqrt{R^2 - (R_0 \sin \ell)^2}$ term in Equation 2. Physically, a single line-of-sight within the solar circle intersects a circular orbit at two distinct points, providing two possible distance solutions that we often alternate between across the TP circle. We also note that portions of the TP circle's circumference are outlined in white, indicating regions of low KD error. This indicates that some points genuinely located on the TP circle are assigned accurate distances using the KD method.

In the bottom, right corner of Fig 1, we isolate zones of low KD error ($|(d_{\rm k} - d_{\rm true})/d_{\rm true}| < 0.02$) in red. These low KD error zones have a spiral-like structure; however, they do not consistently align with the location of gas spiral arms. Previous studies using 2D isothermal simulations have reported that low KD error zones trace gas density peaks along spiral arms [52]. Our result is strikingly different. We attribute the difference in results to our use of 3D models. In 2D, gas is confined to the $z = 0$ plane. When gas encounters spiral-arm shocks, it cannot move vertically and is instead compressed into the gravitational potential minimum of the arms. This limits the development of non-circular streaming motions and therefore keeps KD errors low along the arms. In our 3D models, by contrast, gas can move vertically as well as in the plane; shocks thus induce stronger non-circular motions, leading to higher KD errors along the arms. Overall, this emphasises the need for better developed models, with more advanced gas physics, in order to better constrain kinematic distances errors in the Galaxy.

2 Low KD error zone along bar shock front

In the gas density projection of Fig. 1 (top right panel), the *bar shock fronts*, or dust lanes, are clearly visible and labelled. These are dense structures that occur along the leading sides of the bar, where inflowing gas is compressed by bar-driven shocks. While we adopt the term "shock front" because shocks are present in our model, this feature could also be described as a "compression front" because the finite simulation

resolution limits how fully developed and sharply defined the resulting shock structure can appear.

In the bottom right panel of Fig. 1, we see a distinct low KD error zone that runs adjacent to the bar shock front. A zoomed-in view of this area is shown in Fig. 2, where the low-error zone is seen to trace the bar shock front, wrap around the nuclear spiral arms, and extend throughout the high-density region of the nuclear disc. This feature is not unique to this snapshot ($t = 3.95$ Gyr), but present for most barred snapshots in the model (see Fig. A1).

In Fig. 2 we also map this low KD error zone along the bar into $(\ell, V_{\rm los})$ space. The central low-error region within the nuclear ring corresponds to a diagonal ridge spanning the full range of $V_{\rm los}$ values. For Quadrant I ($0° < \ell < 90°$), we isolate the low KD–error region that follows the bar's shock front and colour it using the `turbo` colormap to illustrate how different positions along the shock front project into $(\ell, V_{\rm los})$ space. Dark blue highlights points near the outer end of the bar, transitioning to dark red toward the bar's centre. For Quadrant IV ($-90° < \ell < 0°$), we simply keep the low–error zone in red.

In Quadrant I, the low-error zone that traces the nuclear spiral arm and dust lane appears as a loop-like structure at $\ell > 0$. Specifically, starting near the inner edge of the shock front and moving outward, the corresponding feature in $(\ell, V_{\rm los})$ space rises from near-zero $V_{\rm los}$ to a secondary peak ($V_{\rm los} \approx 150$ km/s), then declines again as it approaches the bar's outer edge. Importantly, the second peak in the $(\ell, V_{\rm los})$ distribution corresponds to the point in (x, y) space where the tangent-point circle intersects the bar dust lane.

The presence of a low KD error zone along the bar in our simulation does not imply a corresponding feature in the real Galaxy. Nevertheless, projecting the simulated shock front into $(\ell, V_{\rm los})$ space is valuable for better constraining the location of the Galactic bar's dust lanes.

3 $V_{\rm los}$ around the tangent-point circle

In Fig. 3, we present the same $(\ell, V_{\rm los})$ diagram shown in Fig. 2 for the $t = 3.95$ Gyr snapshot. This time, however, we overlay magenta points representing the mean $V_{\rm los}$ along the tangent-point circle. This was computed by: (i) Producing a mass-weighted two-dimensional projection of $V_{\rm los}$ along the z-axis (top-left panel of Fig. B2). (ii) Constructing a ring of thickness 0.1 kpc extending from the Sun's position at $(8.5, 0)$ to the Galactic centre, and calculating the mean $V_{\rm los}$ within the ring as a function of Galactic longitude ℓ (using the 2D map).

There are significant streaming motions in the simulation. While this streaming does settle toward the end of the model (ie. at $t = 3.95$ Gyr), it is still present. This was demonstrated in Figure 19 of [48], where the tangent-point method produces significant errors when used to recover underlying azimuthally-averaged circular rotation curves of the model, precisely because of the streaming associated with the bar and spiral arms.

Given the non-circular motions in the $t = 3.95$ Gyr snapshot, it may be surprising that the magenta points in Fig. 3 closely trace the outer envelope of the $(\ell, V_{\rm los})$

distribution. This suggests that the line-of-sight velocities along the tangent-point circle lie near the terminal velocities, despite the underlying streaming motions.

To interpret this result, we must distinguish between the two directions of mapping: from (x, y) to $(\ell, V_{\rm los})$, and from $(\ell, V_{\rm los})$ back to (x, y). In our model, the presence of non-circular motions means that points on the terminal velocity envelope (i.e., the outer envelope of the $(\ell, V_{\rm los})$ diagram) do not map cleanly onto the tangent-point circle in (x, y) space (see Fig. 13 of [48]). However, the reverse mapping behaves differently: when points along the tangent-point circle are projected into $(\ell, V_{\rm los})$ space, they do not trace the terminal envelope exactly, but they do consistently lie close to it (see Fig. 3). This proximity arises because the Galaxy is rotationally dominated: even in the presence of substantial streaming motions, the radial velocity component, v_R, remains relatively small ($\sim$0–30 km/s) compared to the azimuthal component v_ϕ. As a result, the projection of the gas velocity vector onto the line-of-sight still yields a large $V_{\rm los}$, due to geometric effects, even if it does not represent the maximum possible $V_{\rm los}$ along a given line of sight.

The close correspondence between $V_{\rm los}$ values along the tangent-point (TP) circle and the terminal velocity envelope implies that the intersection of the TP circle with the bar must leave a distinct signature in the terminal curve. When the TP circle intersects the bar region, there are distinct changes in v_R and v_ϕ for gas in the bar region, which will affect the corresponding $(\ell, V_{\rm los})$ values. As we follow the terminal velocity envelope from large positive longitudes (e.g. $\ell \approx 60°$) toward smaller values, $V_{\rm los}$ varies smoothly until reaching a secondary peak (at $V_{\rm los} \approx 150$ km/s). Beyond this point, the curve exhibits a sharp drop, followed by a rapid rise to the global maximum at low longitudes. Following this logic, we suspect that the second peak in $(\ell, V_{\rm los})$ diagrams corresponds to the bar-TP intersection point. We explore this hypothesis in the sections that follow.

4 Intersections between the Tangent-point circle and Bar Dust lanes using Kinematic Distances and Masers

To test this hypothesis, we take an $(\ell, V_{\rm los})$ diagram for a representative snapshot in our model, identify the second peak (at $\ell > 0$), and project its coordinates back into (x, y) space to check whether it coincides with the TP–bar dust lane intersection. Comparable results are obtained for most times in the simulation. This projection can be performed using two similar methods:

- The Kinematic Distance Method. Substitute the $(\ell, V_{\rm los})$ coordinate of the second peak into the kinematic distance equations and hence estimate the gas parcel's position in (x, y) space. Since the KD error adjacent to the dust lanes is very low ($< 2\%$) in the simulations, the estimate should be highly accurate.
- Longitude-TP intersection. Determine the longitude of the secondary peak, draw the corresponding line of longitude in (x, y) space, and compute its intersection with the tangent-point circle. If the terminal curve changes sharply where the TP circle meets the dust lane, this intersection should coincide with the secondary peak.

In Fig. 4, we apply both methods to the $t = 3.95$ Gyr snapshot. The right panel marks the first and second $(\ell, V_{\rm los})$ peaks with cyan and lime green points, while the left panel shows their (x, y) positions computed with the kinematic distance method. In the (x, y) panel, we also overlay the TP circle (white dashed) and lines of longitude for both peaks (black dashed). The lime green points lie exactly at the TP circle–bar dust lane intersection, confirming that the second peak in $(\ell, V_{\rm los})$ maps to this location at $t = 3.95$ Gyr in the model. Both described methods accurately recover this intersection point.

In observations, even if a low KD error zone does not exist along the Galactic bar dust lane, we still expect a sudden change in $V_{\rm los}$ to occur when the TP circle intersects the bar, and for this to be encoded in the second peak of the terminal velocity curve for Quadrant I. This expectation arises because $V_{\rm los}$ values along the TP circle closely resemble the terminal curve values in simulations, and probably do in observations as well. Therefore, we argue that these methods remain effective for studying the bar, even without a low KD error zone adjacent to the dust lane.

5 The Norma arm traces Galactic bar shock front

We have already demonstrated the success of our method in locating the TP–bar intersection within the simulation. Now we apply the same methods to CO $(\ell, V_{\rm los})$ observations. We begin by visually identifying the second peak in the CO data from [53]. Columns 1 and 2 of Table 1 list the $(\ell, V_{\rm los})$ coordinates of the second peaks identified via visual inspection. In Quadrant IV, both a second and third peak are apparent. We suggest that the third peak arises from a spiral arm crossing the TP circle at more negative longitudes, prior to the circle's intersection with the bar dust lane. This feature is not the focus of the present work, but we plan to investigate it in future work on bar–spiral arm attachment.

The second peak in Quadrant I of the CO observations is located at $(\ell, V_{\rm los}) = (22^\circ, 124\ {\rm km\,s^{-1}})$. We apply both the kinematic distance method and the longitude–TP intersection method to estimate the corresponding (x, y) coordinates. The results are shown in Fig. 5, alongside other observational constraints on the bar region.

The top left panel of Fig. 5 shows the location of high-mass star-forming regions with measured trigonometric parallaxes from [1]. The grey ellipse is used by [1] to indicate the approximate location of the long bar, but is not particularly important for this work. The red, blue, cyan and magenta curves show the hypothesised locations for the four major spiral arms, which are found by fitting log-periodic spirals to the maser locations [1]. We are most interested in the red scatter points with black outline, which [1] identifies to be part of the Norma spiral arm.

The top right panel of Fig. 5 shows the (x, y) gas density projection at $t = 3.95$ Gyr in the simulation. The darker red points are the low KD error zone along the bar shock front, previously discussed in Fig. 2. Similar to Fig. 2, we colour the low KD error zone along the bar shock front in Quad I `turbo`. This makes it easier to see the correspondence between individual points in (x, y) and $(\ell, V_{\rm los})$ space. The lighter red points with black outlines mark masers from [1], associated with the Norma spiral arm. The white dashed circle represents the tangent-point circle, while white dashed

lines show the lines of longitude corresponding to the second and third peaks in the CO $(\ell, V_{\rm los})$ observations from [53]. These longitude lines are labelled accordingly. The gold scatter point with black outline (for the second peak in Quad I), or equivalently the black scatter points (for Quad IV) denote the estimated (x, y) coordinates of the TP–bar dust lane intersection, derived using the kinematic distance method with $R_0 = 8.15$ kpc and $\Theta_0 = 236\ {\rm km\,s^{-1}}$, as recommended by [1].

These gold and black points coincide precisely with the intersections of the TP circle and the relevant lines of longitude. In practical terms, the gold point with black outline in Quadrant I marks our estimate of where the TP circle intersects the Galactic bar in the Milky Way.

In the top-right panel of Fig. 5, this gold Quadrant I point aligns closely with the "Norma" arm masers from [1]. We argue instead that these masers trace a shock front along the Galactic bar. Moreover, the curvature traced by the masers and extending through the gold point closely resembles that of the simulated bar shock front (`turbo` coloured points). If both the masers and the gold point indeed trace the bar's shock front, this suggests that the Galactic bar is slightly larger than the bar in our model.

The second row of Fig. 5 presents the location of the bar shock front in $(\ell, V_{\rm los})$ space. The left-middle panel presents the observed HI $(\ell, V_{\rm los})$ distribution in the Milky Way [1]. The light red points with black outline mark the "Norma-arm" masers from [1], while the gold point indicates the second peak estimated from the CO observations of [53]. In Fig. 5, we see that this gold point is also located at a distinct peak in the HI $(\ell, V_{\rm los})$ observations. This is unsurprising because the CO and HI terminal curves are known to be extremely similar to each other in this longitude range [54]. Importantly, the gold point aligns closely with the Norma-arm masers in $(\ell, V_{\rm los})$ space, further supporting our hypothesis that these masers trace the Galactic bar shock front rather than being a distinct spiral arm.

In the right panel of the second row, we present the simulated $(\ell, V_{\rm los})$ distribution for $t = 3.95$ Gyr, corresponding to the simulated (x, y) gas distribution presented in the first row. The `turbo` and dark red coloured points are the low KD error zone tracing the bar shock front from the model. The lighter red scatter points with black outline are the "Norma arm" masers from [1]. Once again, comparing the bar shock front trace in $(\ell, V_{\rm los})$ space to the maser observations, we see that the masers could be consistent with a bar shock front at a slightly larger radius than what is present at $t = 3.95$ Gyr in the model. In $(\ell, V_{\rm los})$ space, the simulated shock front extends from the dark blue points at low longitudes (near zero) up to the light green points at the second peak; similarly, the observed masers extend from a position close to the dark blue points up to the gold point, which is the second peak in observations [53].

A bar dust lane with similar curvature to the one in our simulations, but associated with a bar that is physically bigger in size, would follow a trace comparable to the "Norma" arm masers in $(\ell, V_{\rm los})$ space. The increased bar size shifts the dust-lane signature to higher longitudes, while the curvature followed by the masers remains consistent with that of the simulated dust lane. The second peak from observations (gold point) occurs at significantly lower $V_{\rm los}$ than the simulated second peak. This may reflect differences in bar-spiral attachment, or bar pattern speed, between simulations and the actual Galaxy.

Table 1 The coordinates of the second and third peaks in the CO $(\ell, V_{\rm los})$ observations of [53] (their Figure 3). We also include the corresponding (x_k, y_k) positions of gas estimated using the kinematic distance method (found with $R_0 = 8.15\,{\rm kpc}$ and $\Theta_0 = 236\,{\rm km\,s^{-1}}$). In Quadrant I, only the first and second peaks are present. Quadrant IV also has a third peak, but this is not the focus of the present work.

Peak	ℓ (deg)	$V_{\rm los}$ (km s^{-1})	$d_{\rm k}$ (kpc)	$x_{\rm k}$ (kpc)	$y_{\rm k}$ (kpc)
Second peak Quad I	22°	124	7.56	-1.14	2.83
Second peak Quad IV	−16.5°	−150	7.81	-0.66	-2.22
Third peak Quad IV	−28°	−111	7.20	-1.79	-3.38

The bottom row shows stellar density distributions. The bottom left panel is the hypothesised stellar density distribution from [32], which is based off observations of red clump giants stars from the United Kingdom Infrared Deep Sky Survey (UKIDSS) [55], the Two Micron All Sky Survey (2MASS) [56], the Vista Variables in the Via Lactea (VVV) survey [57] and the Galactic Legacy Infrared Mid-Plane Survey Extraordinaire [58]. The black scatter point, with white outline, represents our predicted TP-bar dust lane intersection point in the Milky Way. Our predicted location of this intersection point is somewhat consistent with [32], except our predictions suggest the bar is slightly wider (larger semi-major axis). The bottom right panel shows the stellar density distribution at $t = 3.95$ Gyr in the model. We can see that the modelled bar at this time is significantly shorter and thinner than the one hypothesised by [32]. For the reasons above, we argue that the Galactic bar is slightly longer and fatter than the bar in our model at $t = 3.95$ Gyr,

6 Constraining Galactic bar size and angle

Shocks frequently occur at the cusped x_1 orbit. The apocentres of the outermost x_2 orbits graze the pericentre of the cusped x_1 orbit, generating shocks that convert atomic gas into molecular form, and drive gas inflow into the x_2 family [9, 6, 11]. Consequently, shock fronts—typically observed as dust lanes along the bar—can be regarded as lying near the cusped x_1 orbit and the innermost members of the x_1 orbit family (see [12], Fig. 10 for a diagram).

Additionally, there is no universally accepted definition of bar length; there is no precise criterion for where a bar begins and ends nor a standard method for its measurement [49]. Instead, various methods are commonly used, including Fourier decomposition (e.g., [59, 36, 32]), ellipse fitting [60, 32], and overdensity contour mapping [36]. These methods often produce different estimates for the same intrinsic bar length. In this work, we define the bar length as the semi-major axis of the cusped x_1 orbit, $a_{\rm bar}$. The corresponding semi-minor axis, $b_{\rm bar}$, provides additional constraints on bar size and the curvature of associated dust lanes.

If the Norma arm truly does trace the Galactic bar shock front in Quadrant I, this provides a strong constraint on bar size. In Fig. 6, we start with the (x, y) gas density distribution from the $t = 3.95$ Gyr snapshot in the model, previously shown. However, this time, we scale and rotate the simulated (x, y) distribution so that its shock front aligns with the Norma arm (red points with black outline) and the estimated TP-bar

dust lane intersection (gold point with black outline). In Fig. 6, the orange points display the low KD error shock front that has been scaled and rotated to match the observations. We see that the "Norma" arm masers closely trace the simulated shock front.

In the right panel of Fig. 6, we determine the size and rotation angle of the scaled simulation snapshot. The cusped x_1 orbit should approximately follow the dust lanes and enclose the low-density shock cavity. Cyan lines mark the estimated semi-major and semi-minor axes of the low density shock cavity. We also rotated the (x, y) density distribution to achieve the best alignment possible with the Norma masers.

Based on visual inspection, the Norma masers fit the bar shock front best when the stellar bar angle is $\phi \approx 20°$. Very small variations on either side of this angle still provide a reasonable fit. However, this supports a relatively low Galactic bar inclination, likely $\phi \lesssim 25°$. This is significantly less than the estimates from [61, 32] who argue: $\phi_{bp} = 27° \pm 2°$ for the boxy/peanut bulge and $\phi_{lb} = 28° - 33°$ for the long bar [62].

Additionally, we use the cyan lines in Fig. 6 to estimate the bar dimensions: $a = 4.3$ kpc and $b = 2.3$ kpc. These are consistent with the thin-bar estimate of $R_{\rm b} = 4.6 \pm 0.3$ kpc from [32], though slightly on the lower end. We emphasise that some uncertainty naturally arises due to different definitions of bar length. Overall, our results are in support of a longer, fatter Galactic bar. We suggest that allowing the model to evolve beyond $t > 3.95$ Gyr could naturally produce a bar of similar dimensions because the simulated bar grows and slows over time (see [48]).

7 Star formation in the bar

A key result of this work is that the association of "Norma" arm masers with the Galactic bar shock front strongly indicates that star formation occurs within the Milky Way's bar. Masers in the Norma arm are well-established tracers of massive star formation, and their "ages" reflect the evolutionary stage of the stars and molecular clouds hosting them. Most of the masers mapped in the Norma arm [1] are water (H_2O) and methanol (CH_3OH) masers (eg. from the BeSSeL Survey using the VLBI and Japanese VERA project). These are associated with very young star-forming regions ($<<$ 1 Myr), which remain very close to the gas clouds in which they formed because they have not had sufficient time to migrate away [1, 2]. Thus, the presence of masers along the bar shock front provides compelling evidence that the bar is an active site of star formation.

This finding contrasts with trends observed in local barred galaxies, where star formation is often suppressed within the bar compared to the spiral arms. For example, NGC 3351 and NGC 1512 show virtually no star formation within the bar region, despite the presence of prominent H II regions concentrated in the nuclear disc and in an inner ring, at larger radii, that encircles the bar [63, 13]. In NGC 4303, the star formation rate and efficiency in the spiral arms are roughly twice those in the bar [17], and in NGC 5383, while some star formation occurs along the dust lanes, the SFR remains low relative to the nuclear regions and bar ends [16].

Nevertheless, counterexamples exist, with bars in some nearby galaxies displaying significant star formation along their dust lanes. NGC 7479 hosts a strong bar with intense star formation along its length, likely linked to a recent minor merger that left the bar in a transitional phase, sustaining star formation along the bar while also feeding the nuclear ring [64, 65, 66, 67]. Additionally, NGC 3359 shows chains of bright H II regions along its young ($\sim$ 400 Myr) bar, which likely still contains ample gas due to its age [68, 20]. Furthermore, NGC 2903 has HII distributed along its young bar, but its dust lanes also have a broken feathery structure, which weakens shear and shocks [69, 70]. Star formation may also occur in dust spurs. For instance, NGC 1530, which hosts one of the strongest known bars ($\sim$ 24 kpc) with straight dust lanes [71], contains HII regions on both trailing and leading sides of the main dust lane. Age differences between these regions suggest that massive stars form in dust spurs on the trailing side and later migrate to the leading side [72]. Similarly, in NGC 5383, star formation within the main dust lanes is minimal, but the few HII regions along the bar are linked to dust spurs [16].

If star formation does occur in the Milky Way's bar, a key question is what mechanism drives this. One possibility is that dust spurs host star formation, perhaps corresponding to structures identified as Bania's clumps in $(\ell, V_{\rm los})$ diagrams [4]. However, the very young ages ($\ll$ 1 Myr) of the star-forming regions associated with the "Norma" arm masers make this scenario unlikely. In NGC 1530, an age offset of $\approx$ 1.5–2.5 Myr between H II regions on the trailing and leading sides of the bar dust lane suggests that stars may form on the trailing side and subsequently migrate toward the leading side [72]. By contrast, the young star-forming regions linked to the "Norma" arm masers closely coincide with the gas clouds in which they originate. A more plausible explanation for star formation in the Galactic bar is that the curved distribution of the "Norma" arm masers—or alternatively the bar shock front—reflect a weaker bar, where shear and shocks are insufficient to fully suppress star formation. Additionally, even if star formation occurs along the Galactic bar dust lanes, we do not know how the SFR and SFE in the dust lanes compare to those in the nuclear disc and at the bar ends — whether star formation in the bar is still somewhat suppressed, or not.

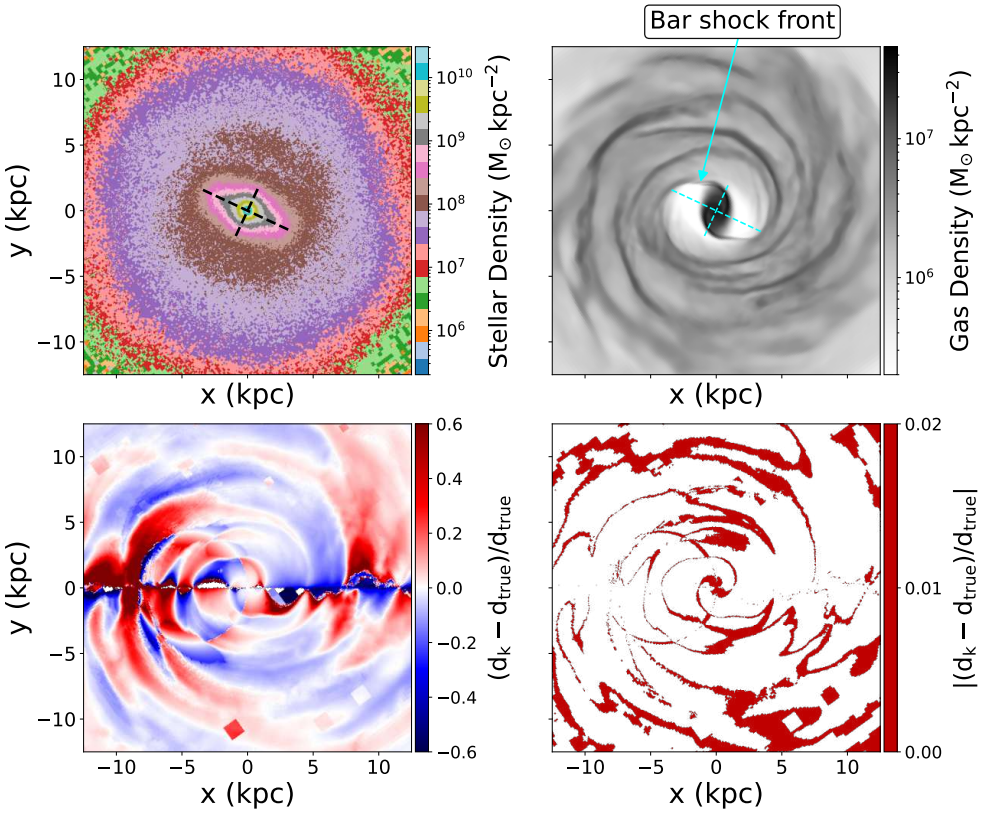


Fig. 1 Top row shows stellar density (left) and gas density (right) at $t = 3.95$ Gyr in the model. The black dashed lines overlaid on the stellar density projection, and the cyan dashed lines on the gas, indicate the bar's semi-major and semi-minor axes. The bar has an inclination angle of 25 deg relative to the $x = 0$ axis. Bottom row shows kinematic distance error map on the left. The bottom panel shows low KD error zones ($|(d_{\rm k} - d_{\rm true})/d_{\rm true}| < 0.02$) in red.

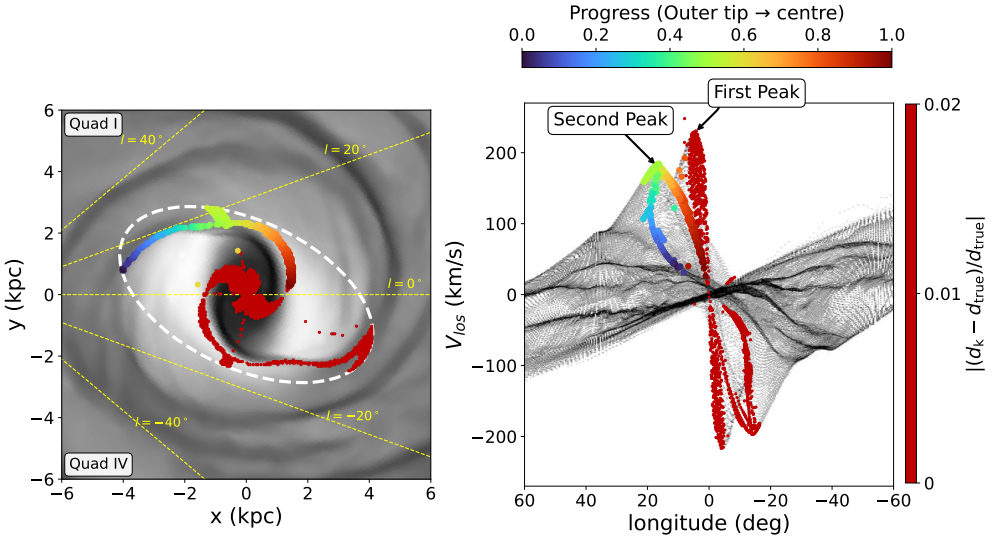


Fig. 2 Left panel shows the (x, y) gas density distribution at $t = 3.95$ Gyr in the model. In red, we have isolated the the low KD error zone within the bar region, masking out all low error zones outside the white dashed ellipse. Right panel shows the corresponding $(\ell, V_{\rm los})$ diagram. The red points are the low KD error points in the bar region, mapped into $(\ell, V_{\rm los})$ coordinate space.

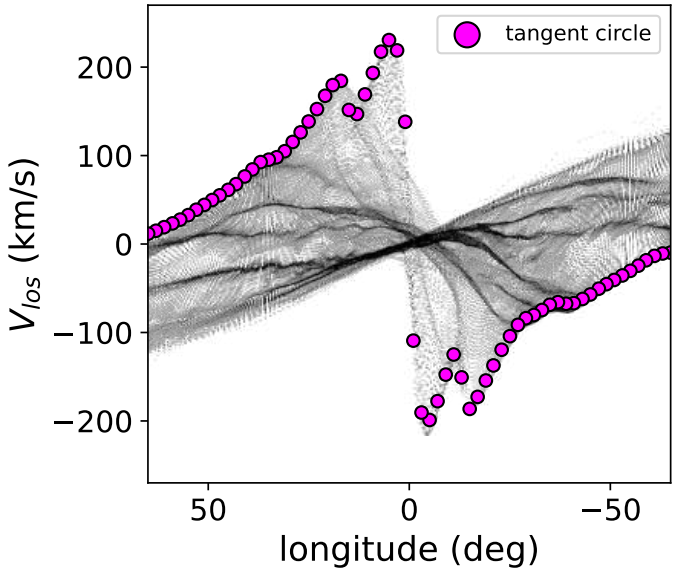


Fig. 3 The $(\ell, V_{\rm los})$ diagram for $t = 3.95$ Gyr in the model. The magenta points overlaid on this represent the mean $V_{\rm los}$ values computed along the tangent-point circle. The magenta points trace the terminal velocity envelope of the underlying $(\ell, V_{\rm los})$ distribution closely.

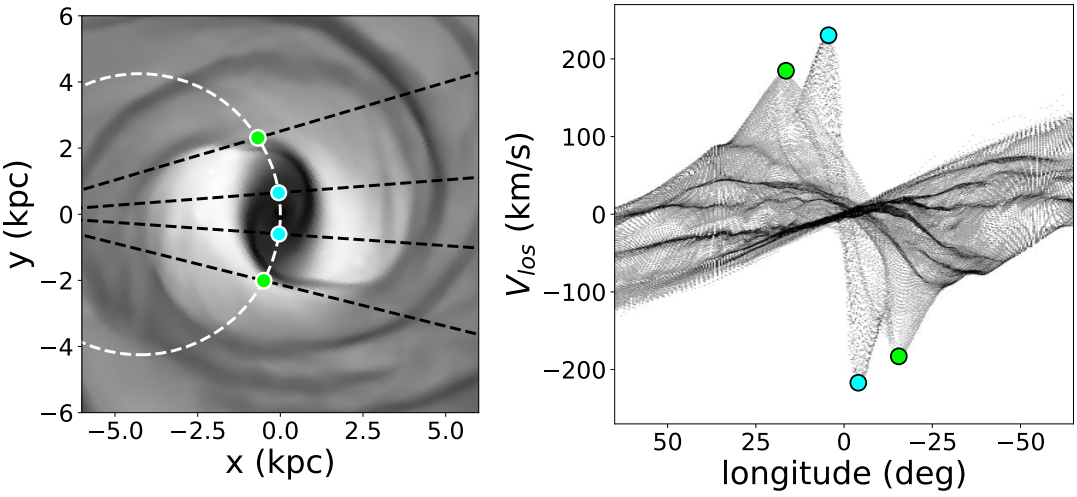


Fig. 4 Left panel shows (x, y) gas density distribution for $t = 3.95$ Gyr snapshot. Right panel is the corresponding $(\ell, V_{\rm los})$ distribution. Cyan and lime green points mark the location of the first and secondary $(\ell, V_{\rm los})$ peaks. We use the kinematic distance method to estimate the (x, y) location corresponding to these peaks, with the result presented using the lime and cyan markers in the left panel. In (x, y), the tangent-point circle (white dashed) and lines-of-longitude corresponding to the peaks (black dashed) are also overlaid.

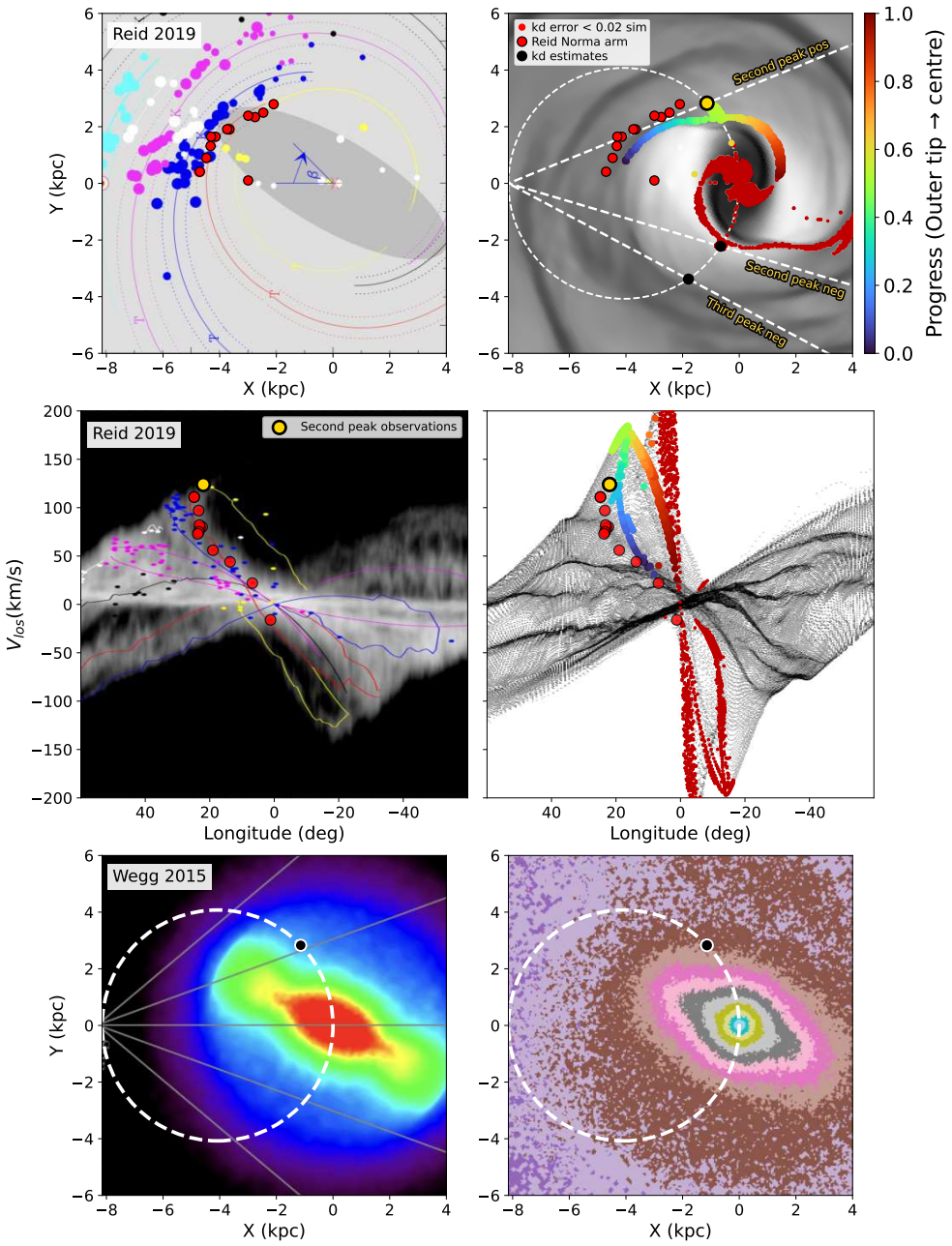


Fig. 5 In the top row, we have: distribution of HMSFRs from [1] on the left, and gas density distribution from $t = 3.95$ Gyr of the model on the right. Over the simulated (x, y) gas density distribution, we overlay zones of low KD error ($< 2\%$) with the red scatter points (no outline), HMSFRs from Norma arm of [1] as the red scatter points with black outline, and the black points are the (x, y) values we estimate correspond to the various peaks in $(\ell, V_{\rm los})$ space. In the second row: we have the $(\ell, V_{\rm los})$ diagram from [1], with the location of the second peak given by the gold marker; the $(\ell, V_{\rm los})$ diagram from the simulation, with low KD error zones in red scatter points(no outline), and HMSFRs in red with black outline. In the bottom panel, we have the estimated stellar density distribution from [32], and the (x, y) stellar density distribution from the model.

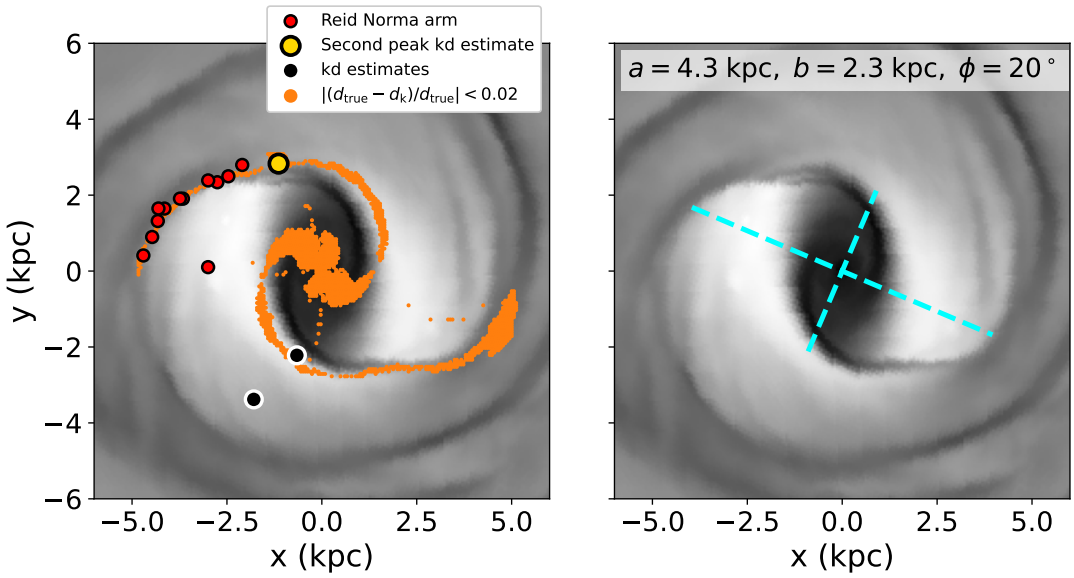


Fig. 6 We have rotated and scaled the (x, y) gas density distribution from the $t = 3.95$ Gyr snapshot of the simulation, such that the simulated shock front coincides with the observations as closely as possible. The orange points represent the rotated and scaled low KD error zone from the simulation. The red scatter points with black outline are the masers traditionally identified with the Norma arm. The black scatter points with white outline are our estimates for intersection points between the tangent-point circle and the bar dust lanes, or alternatively intersection of the cirlce with a spiral arm. On the right panel, we overlay cyan dashed lines across the approximate location of the semi-major and semi-minor axis for the low density shock cavity in the scaled simulation snapshot. In this way, we estimate the Galactic bar size.

Table 2 Galaxy model parameters. Columns 1 and 2 identify the galactic components and their associated functional forms; we note that these are approximations because they share the same gravitational potential. The total mass, scale length, and cut-off radius are indicated in columns 3, 4, and 5 respectively. Column 6 is the number of particles used to sample the corresponding component. Note that for gaseous components, this number corresponds only to the initial particle number.

Component	Profile	Total mass (10^{10}M$_\odot$)	Radial scalelength (kpc)	Cut-off radius (kpc)	Particle count (10^6)
DM halo	NFW	118	19	250	1
Stellar bulge	Hernquist	1.25	0.6	2.0	0.1
Stellar disc	Exp, sech^2	4.31	2.5	25	1
Gas disc	Exp, sech^2	0.46	3.5	–	2

Notes: The NFW and Hernquist functions are defined elsewhere [73, 74]. The scaleheight of the stellar disc is $z_t \approx 300$ pc. The gas disc is initially isothermal with $T = 10^3$ K. The initial gas metallicity is set to $Z = 1$ Z$_\odot$ in the disc, and to zero elsewhere. The gas disc merges smoothly with the background density ($\rho = 10^{-20}$ cm^{-3}, $T = 10^6$ K). The disc-to-total mass fraction is $f_{\rm disc} \approx 0.45$, which renders the disc bar-unstable from the outset [75, 76].

8 Methods

8.1 N-body, hydrodynamic simulation

We focus on one N-body, hydrodynamic simulation of a Milky Way-like galaxy. The Galaxy is approximated by a four-component system, which consists of: 1) a host dark-matter (DM) halo; 2) a central 'classical', pre-assembled stellar bulge; 3) a pre-assembled stellar disc; 4) a gaseous disc, made up of a monoatomic, ideal gas. All components are reactive, i.e. they carry self-gravity and respond dynamically to changes in the potential. The mass and structural properties of each component are summarised in Tab. 2.

The simulations have been set up and run with the Nexus framework [77]. Specifically, the initial conditions for the Galaxy model have been created with an extended version of the agama library [78] that allows the treatment of gaseous component in addition to collisionless components. The initial conditions have been evolved with the adaptive mesh refinement (AMR), N-body/hydrodynamical code Ramses [79]. We evolve the composite system for roughly 4.3 Gyr in a cubic box of size 600 kpc per side, adopting a maximum refinement level $l = 14$, implying a maximum spatial resolution of 600 kpc / $2^{13} \approx 74$ pc.

The gas is subject to radiative cooling and to heating, and it is allowed to form stars, accounting for their evolution, chemical enrichment, and feedback to their environment [80]. This simulation has already been discussed in detail in both [77] and [48].

8.2 The Kinematic Distance Method

Accurately determining distances to the gaseous component of the Milky Way remains a significant challenge. At heliocentric distances less than approximately 10 kpc,

trigonometric parallaxes to maser sources are widely regarded as the "gold standard" distance method, providing the most accurate measurements [81, 82, 83]. Beyond this range, and on the far side of the Galactic centre especially, kinematic distance estimates are more commonly used [84, 52].

The KD method estimates the galactocentric radius for a parcel of gas by combining its line-of-sight velocity, $V_{\rm los}$, with an assumed Galactic rotation curve, $(R, \Theta(R))$:

$$R = R_0 \sin(\ell) \frac{\Theta(R)}{\Theta_0 \sin(\ell) + V_{\rm los}} \tag{1}$$

where R_0 is the sun's distance from the Galactic centre, Θ_0 is the sun's circular velocity, ℓ is Galactic longitude, and $V_{\rm los}$ is line-of-sight velocity. The estimated galactocentric radius is then used to compute a kinematic distance:

$$d_{\rm k} = R_0 \cos(\ell) \pm \sqrt{R^2 - (R_0 \sin(\ell))^2} \tag{2}$$

When $V_{\rm los} < -\Theta_0 \sin \ell$, the estimated Galactocentric radius becomes negative, and these points are therefore excluded from our analysis. Furthermore, d_k is undefined when $[R^2 - (R_0 \sin(\ell))^2] < 0$. Hence, the square root is set to zero, in these cases, placing the corresponding points at the tangent-point.

Unfortunately, KD estimates rely on the assumption of circular motion. Non-axisymmetric structures (eg. bar, spiral arms) introduce significant errors as a result of their associated streaming motions [85, 86, 87, 81].

Acknowledgements. TTG acknowledges financial support from the Australian Research Council (ARC) through an Australian Laureate Fellowship awarded to JBH. The computations and data storage were enabled by two facilities: (i) the National Computing Infrastructure (NCI) Adapter Scheme, provided by NCI Australia, an NCRIS capability supported by the Australian Government; and (ii) LUNARC, the Centre for Scientific and Technical Computing at Lund University (resource allocations LU 2023/2-39 and LU 2023/12-6). ChatGPT (OpenAI) was used for minor code-editing and figure-presentation suggestions. All suggestions were reviewed and verified by the authors, who take full responsibility for the final content.

Declarations

Funding.

Competing interests. The authors declare no competing interests.

Data Availability. Available on request to corresponding author.

Materials Availability. Available on request to corresponding author.

Author contribution. H.D. planned the project, carried out all the analysis, generated the figures and led the writing of the manuscript. J.B.H supervised the project, engaged in extensive discussion, contributed to the interpretation of results and edited the manuscript. T.T.G. made the simulations, wrote the N-body/hydrodynamic simulation section in the Methods, and engaged in discussion of results. O.A. worked with T.T.G to make the simulations, and provided extensive feedback on both the project and the manuscript.

Appendix A Low KD error zones across time in the bar region

In Fig. A1, we present the (x, y) gas distribution in the inner ≈ 5 kpc for $t = 3.81 - 3.95$ Gyr in our simulation. The red represents zones of very low KD error ($< 2\%$). For most snapshots, there is a low KD error zone tracing the Galactic bar shock front. Occasionally (eg. $t = 3.88 - 3.92$ Gyr), this does not hold true. We propose that such deviations arise when a gaseous spiral arm intersects the tangent-point circle prior (at larger $|\ell|$) to the bar dust lane. We will explore this in future work. Although Fig. A1 presents only a small subset of barred snapshots in the star-forming model, we see similar patterns for most times in the simulation when a bar is present.

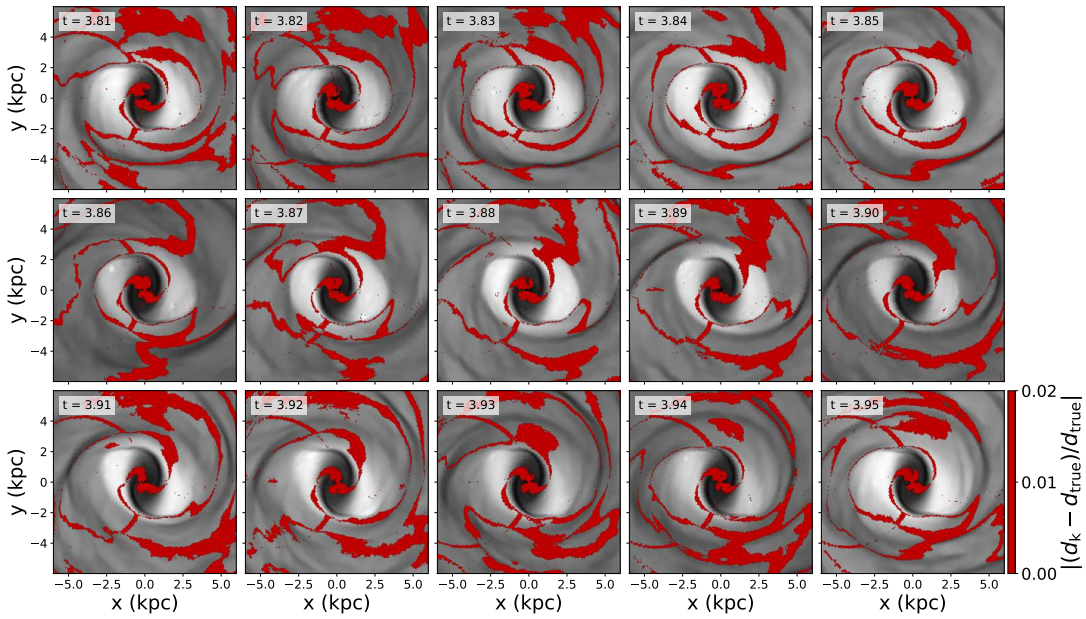


Fig. A1 Low KD error zones for $t = 3.81 - 3.95$ Gyr in the star-forming gas model (red). Low KD error zone tracing along bar shock front is present in most snapshots in a model. When this is not the case, this is often because a spiral arm intercepts the tangent-point circle before it intersects the bar.

Appendix B Line-of-sight velocity and streaming motions

We reproduce Fig. 10 from [52] for $t = 3.95$ Gyr in our simulation. The smallest KD errors arise when $V_{\rm los} - V_{\rm c,los}$ is at a minimum; that is, where the line-of-sight velocity is consistent with the pure circular motion case. This is to be expected because the KD method relies on the assumption of circular motion.

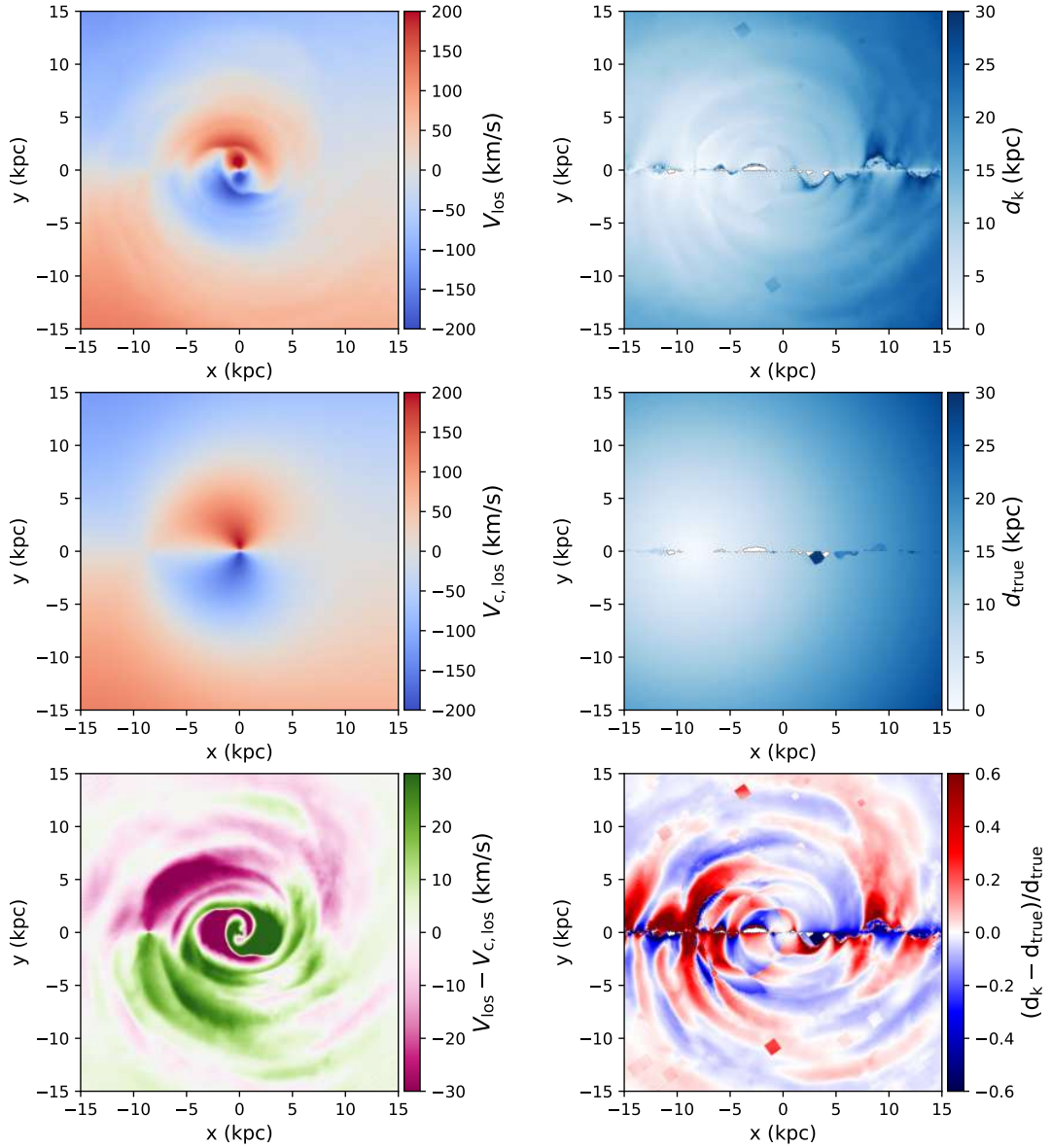


Fig. B2 This is a reproduction of Figure 10 from [52]. The first column presents, from top to bottom: the mass-weighted line-of-sight velocity $V_{\rm los}$ projected along the z-axis, the corresponding $V_{\rm los}$ projection for the case of pure circular motion in an azimuthally-averaged axisymmetric potential, and the difference $V_{\rm los} - V_{\rm c,los}$. The second column shows, from top to bottom: distances estimated with the KD method $d_{\rm k}$, true distances in the simulation $d_{\rm true}$, the resulting KD error.

References

[1] Reid, M. et al. Trigonometric parallaxes of high-mass star-forming regions: our view of the milky way. The Astrophysical Journal **885**, 131 (2019).

[2] Kumar, J. et al. The expanding 3 kpc arms are neither expanding nor spiral arms but x1 orbits driven by the galactic bar. The Astrophysical Journal **982**, 185 (2025).

[3] Hou, L. The spiral structure in the solar neighborhood. Frontiers in Astronomy and Space Sciences **8**, 671670 (2021).

[4] Fux, R. 3D self-consistent N-body barred models of the Milky Way. II. Gas dynamics. A&A **345**, 787–812 (1999). astro-ph/9903154.

[5] Bally, J., Stark, A. A., Wilson, R. W. & Henkel, C. Galactic center molecular clouds. ii-distribution and kinematics. Astrophysical Journal, Part 1 (ISSN 0004-637X), vol. 324, Jan. 1, 1988, p. 223-247. **324**, 223–247 (1988).

[6] Morris, M. & Serabyn, E. The galactic center environment. Annual Review of Astronomy and Astrophysics **34**, 645–701 (1996).

[7] Oka, T., Hasegawa, T., Hayashi, M., Handa, T. & Sakamoto, S. Co (j= 2-1) line observations of the galactic center molecular cloud complex. ii dynamical structure and physical conditions. The Astrophysical Journal **493**, 730 (1998).

[8] Henshaw, J. D. et al. Star formation in the central molecular zone of the milky way. arXiv preprint arXiv:2203.11223 (2022).

[9] Binney, J., Gerhard, O. E., Stark, A. A., Bally, J. & Uchida, K. I. Understanding the kinematics of galactic centre gas. Monthly Notices of the Royal Astronomical Society **252**, 210–218 (1991).

[10] Jenkins, A. & Binney, J. Dynamics of gas near the galactic centre. Monthly Notices of the Royal Astronomical Society **270**, 703–719 (1994).

[11] Gerhard, O. E. Dynamics of the bar at the galactic centre. In Symposium-International Astronomical Union, vol. 169, 79–91 (Cambridge University Press, 1996).

[12] Downes, D., Reynaud, D., Solomon, P. & Radford, S. Co in the barred galaxy ngc 1530. Astrophysical Journal v. 461, p. 186 **461**, 186 (1996).

[13] Kim, T. et al. Impacts of bar-driven shear and shocks on star formation. The Astrophysical Journal **968**, 87 (2024).

[14] Tubbs, A. D. The inhibition of star formation in barred spiral galaxies. Astrophysical Journal, Part 1, vol. 255, Apr. 15, 1982, p. 458-466. **255**, 458–466 (1982).

[15] Reynaud, D. & Downes, D. Kinematics of the gas in a barred galaxy: do strong shocks inhibit star formation? Astronomy and Astrophysics, v. 337, p. 671-680 (1998) **337**, 671–680 (1998).

[16] Sheth, K., Regan, M. W., Vogel, S. N. & Teuben, P. J. Molecular gas, dust, and star formation in the barred spiral ngc5383. The Astrophysical Journal **532**, 221 (2000).

[17] Momose, R., Okumura, S. K., Koda, J. & Sawada, T. Star formation efficiency in the barred spiral galaxy ngc 4303. The Astrophysical Journal **721**, 383 (2010).

[18] Emsellem, E. et al. The interplay between a galactic bar and a supermassive black hole: nuclear fuelling in a subparsec resolution galaxy simulation. Monthly Notices of the Royal Astronomical Society **446**, 2468–2482 (2015).
[19] Maeda, F., Egusa, F., Ohta, K., Fujimoto, Y. & Habe, A. Statistical study of the star formation efficiency in bars: Is star formation suppressed in gas-rich bars? The Astrophysical Journal **943**, 7 (2023).
[20] Martin, P. & Friedli, D. Star formation in bar environments. i. morphology, star formation rates and general properties. Astronomy and Astrophysics, v. 326, p. 449-464 **326**, 449–464 (1997).
[21] Hirota, A. et al. Wide-field 12co (j= 1–0) imaging of the nearby barred galaxy m 83 with nma and nobeyema 45 m telescope: Mole cular gas kinematics and star formation along the bar. Publications of the Astronomical Society of Japan **66**, 46 (2014).
[22] Renaud, F. et al. Environmental regulation of cloud and star formation in galactic bars. Monthly Notices of the Royal Astronomical Society **454**, 3299–3310 (2015).
[23] Beuther, H., Meidt, S., Schinnerer, E., Paladino, R. & Leroy, A. Interactions of the galactic bar and spiral arm in ngc 3627. Astronomy & Astrophysics **597**, A85 (2017).
[24] Law, C. J. et al. Submillimeter array observations of extended co (j= 2- 1) emission in the interacting galaxy ngc 3627. The Astrophysical Journal **865**, 17 (2018).
[25] Athanassoula, E. The existence and shapes of dust lanes in galactic bars. Monthly Notices of the Royal Astronomical Society **259**, 345–364 (1992).
[26] Newnham, L. et al. The h i morphology and stellar properties of strongly barred galaxies: support for bar quenching in massive spirals. Monthly Notices of the Royal Astronomical Society **492**, 4697–4715 (2020).
[27] George, K., Subramanian, S. & Paul, K. Significance of bar quenching in the global quenching of star formation. Astronomy & Astrophysics **628**, A24 (2019).
[28] Scaloni, L. et al. The impact of stellar bars on star-formation quenching: Insights from a spatially resolved analysis in the local universe. Astronomy & Astrophysics **687**, A255 (2024).
[29] Bland-Hawthorn, J., Tepper-Garcia, T., Agertz, O. & Federrath, C. Turbulent gas-rich disks at high redshift: bars and bulges in a radial shear flow. The Astrophysical Journal **968**, 86 (2024).
[30] Haywood, M. et al. When the milky way turned off the lights: Apogee provides evidence of star formation quenching in our galaxy. Astronomy & Astrophysics **589**, A66 (2016).
[31] Khoperskov, S. et al. Why does the milky way have a bar? Monthly Notices of the Royal Astronomical Society **533**, 3975–3986 (2024).
[32] Wegg, C., Gerhard, O. & Portail, M. The structure of the milky way's bar outside the bulge. Monthly Notices of the Royal Astronomical Society **450**, 4050–4069 (2015).
[33] Pérez-Villegas, A., Portail, M., Wegg, C. & Gerhard, O. Revisiting the tale of hercules: how stars orbiting the lagrange points visit the sun.

The Astrophysical Journal Letters **840**, L2 (2017).
[34] Monari, G., Famaey, B., Siebert, A., Wegg, C. & Gerhard, O. Signatures of the resonances of a large galactic bar in local velocity space. Astronomy & Astrophysics **626**, A41 (2019).
[35] Chiba, R. & Schönrich, R. Tree-ring structure of galactic bar resonance. Monthly Notices of the Royal Astronomical Society **505**, 2412–2426 (2021).
[36] Hilmi, T. et al. Fluctuations in galactic bar parameters due to bar–spiral interaction. Monthly Notices of the Royal Astronomical Society **497**, 933–955 (2020).
[37] Vislosky, E. et al. Gaia dr3 data consistent with a short bar connected to a spiral arm. Monthly Notices of the Royal Astronomical Society **528**, 3576–3591 (2024).
[38] Lucey, M. et al. Dynamically constraining the length of the milky way bar. Monthly Notices of the Royal Astronomical Society **520**, 4779–4792 (2023).
[39] Dehnen, W. The effect of the outer lindblad resonance of the galactic baron the local stellar velocity distribution. The Astronomical Journal **119**, 800 (2000).
[40] Antoja, T. et al. Constraints on the galactic bar from the hercules stream as traced with rave across the galaxy. Astronomy & Astrophysics **563**, A60 (2014).
[41] Fragkoudi, F. et al. On the ridges, undulations, and streams in gaia dr2: linking the topography of phase space to the orbital structure of an n-body bar. Monthly Notices of the Royal Astronomical Society **488**, 3324–3339 (2019).
[42] Sormani, M. C., Binney, J. & Magorrian, J. Gas flow in barred potentials. Monthly Notices of the Royal Astronomical Society **449**, 2421–2435 (2015).
[43] Englmaier, P. & Gerhard, O. Gas dynamics and large-scale morphology of the milky way galaxy. Monthly Notices of the Royal Astronomical Society **304**, 512–534 (1999).
[44] Monaghan, J. J. Smoothed particle hydrodynamics. ARA&A **30**, 543–574 (1992).
[45] Weiner, B. J. & Sellwood, J. The properties of the galactic bar implied by gas kinematics in the inner milky way. The Astrophysical Journal **524**, 112 (1999).
[46] Sormani, M. C., Binney, J. & Magorrian, J. Gas flow in barred potentials–iii. effects of varying the quadrupole. Monthly Notices of the Royal Astronomical Society **454**, 1818–1839 (2015).
[47] Li, Z., Shen, J., Gerhard, O. & Clarke, J. P. Gas dynamics in the galaxy: Total mass distribution and the bar pattern speed. The Astrophysical Journal **925**, 71 (2022).
[48] Davis, H., Tepper-Garcia, T., McClure-Griffiths, N., Bland-Hawthorn, J. & Agertz, O. Hi terminal velocity curves–lessons learned from n-body/hydrodynamicsurrogate'models of the milky way. arXiv preprint arXiv:2510.10845 (2025).
[49] Iles, E. J. et al. The impact of bar origin and morphology on stellar migration. **submitted** (2025).
[50] Oort, J. H., Kerr, F. J. & Westerhout, G. The galactic system as a spiral nebula. In A Source Book in Astronomy and Astrophysics, 1900–1975, 643–651 (Harvard University Press, 1979).
[51] Gómez, G. C. Errors in kinematic distances and our image of the milky way

galaxy. The Astronomical Journal **132**, 2376 (2006).
[52] Hunter, G. H. et al. Testing kinematic distances under a realistic galactic potential-investigating systematic errors in the kinematic distance method arising from a non-axisymmetric potential. Astronomy & Astrophysics **692**, A216 (2024).
[53] Dame, T. M., Hartmann, D. & Thaddeus, P. The milky way in molecular clouds: A new complete cosurvey. The Astrophysical Journal **547**, 792 (2001).
[54] McClure-Griffiths, N. & Dickey, J. M. Milky way kinematics. ii. a uniform inner galaxy h i terminal velocity curve. The Astrophysical Journal **831**, 124 (2016).
[55] Lawrence, A. et al. The UKIRT Infrared Deep Sky Survey (UKIDSS). MNRAS **379**, 1599–1617 (2007). astro-ph/0604426.
[56] Skrutskie, M. F. et al. The Two Micron All Sky Survey (2MASS). AJ **131**, 1163–1183 (2006).
[57] Minniti, D. et al. VISTA Variables in the Via Lactea (VVV): The public ESO near-IR variability survey of the Milky Way. **15**, 433–443 (2010). 0912.1056.
[58] Benjamin, R. A. et al. First GLIMPSE Results on the Stellar Structure of the Galaxy. ApJ **630**, L149–L152 (2005). astro-ph/0508325.
[59] Dehnen, W., Semczuk, M. & Schönrich, R. Measuring bar pattern speeds from single simulation snapshots. Monthly Notices of the Royal Astronomical Society **518**, 2712–2718 (2023).
[60] Athanassoula, E. & Misiriotis, A. Morphology, photometry and kinematics of n-body bars—i. three models with different halo central concentrations. Monthly Notices of the Royal Astronomical Society **330**, 35–52 (2002).
[61] Wegg, C. & Gerhard, O. Mapping the three-dimensional density of the galactic bulge with vvv red clump stars. Monthly Notices of the Royal Astronomical Society **435**, 1874–1887 (2013).
[62] Bland-Hawthorn, J. & Gerhard, O. The galaxy in context: structural, kinematic, and integrated properties. Annual Review of Astronomy and Astrophysics **54**, 529–596 (2016).
[63] Phillips, A. C. Star formation in barred galaxies. In International Astronomical Union Colloquium, vol. 157, 44–53 (Cambridge University Press, 1996).
[64] Laine, S. & Gottesman, S. Neutral hydrogen gas distribution and kinematics in ngc 7479. Monthly Notices of the Royal Astronomical Society **297**, 1041–1051 (1998).
[65] Rozas, M., Zurita, A., Heller, C. & Beckman, J. Global properties of the population of hii regions in ngc 7479 from photometric hα imaging. Astronomy and Astrophysics Supplement Series **135**, 145–158 (1999).
[66] Zhou, Z.-M., Cao, C., Meng, X.-M. & Wu, H. Star formation properties in barred galaxies (sfb). i. ultraviolet to infrared imaging and spectroscopic studies of ngc 7479. The Astronomical Journal **142**, 38 (2011).
[67] Quillen, A. et al. An estimate of the gas inflow rate along the bar in ngc 7479. arXiv preprint astro-ph/9409033 (1994).
[68] Martin, P. & Roy, J.-R. The oxygen distribution in ngc 3359 or a disk galaxy in the early phase of bar formation.

The Astrophysical Journal, Part 1 (ISSN 0004-637X), vol. 445, no. 1, p. 161-172 **445**, 161–172 (1995).

[69] Leon, S. et al. Hcn (1–0) enhancement in the bar of ngc 2903. Astronomy & Astrophysics **491**, 703–711 (2008).

[70] Popping, G., Pérez, I. & Zurita, A. Multiwavelength study of the star-formation in the bar of ngc 2903. Astronomy & Astrophysics **521**, A8 (2010).

[71] Block, D. et al. Gravitational bar and spiral arm torques from ks-band observations and implications for the pattern speeds. The Astronomical Journal **128**, 183 (2004).

[72] Zurita, A. & Pérez, I. Where are the stars of the bar of ngc 1530 forming? Astronomy & Astrophysics **485**, 5–20 (2008).

[73] Navarro, J. F., Frenk, C. S. & White, S. D. M. A Universal Density Profile from Hierarchical Clustering. ApJ **490**, 493–+ (1997).

[74] Hernquist, L. An analytical model for spherical galaxies and bulges. ApJ **356**, 359–364 (1990).

[75] Fujii, M., Bédorf, J., Baba, J. & Portegies Zwart, S. The dynamics of stellar discs in live dark-matter haloes. Monthly Notices of the Royal Astronomical Society **477**, 1451–1471 (2018).

[76] Bland-Hawthorn, J., Tepper-Garcia, T., Agertz, O. & Freeman, K. The Rapid Onset of Stellar Bars in the Baryon-dominated Centers of Disk Galaxies. ApJ **947**, 80 (2023).

[77] Tepper-García, T. et al. NEXUS: A framework for controlled simulations of idealised galaxies. MNRAS (2024).

[78] Vasiliev, E. AGAMA: action-based galaxy modelling architecture. MNRAS **482**, 1525–1544 (2019).

[79] Teyssier, R. Cosmological hydrodynamics with adaptive mesh refinement. A new high resolution code called RAMSES. A&A **385**, 337–364 (2002).

[80] Agertz, O. et al. VINTERGATAN - I. The origins of chemically, kinematically, and structurally distinct discs in a simulated Milky Way-mass galaxy. MNRAS **503**, 5826–5845 (2021).

[81] Reid, M. J. On the accuracy of three-dimensional kinematic distances. The Astronomical Journal **164**, 133 (2022).

[82] Wenger, T. V., Balser, D. S., Anderson, L. & Bania, T. Kinematic distances: a monte carlo method. The Astrophysical Journal **856**, 52 (2018).

[83] Reid, M. et al. Trigonometric parallaxes of high mass star forming regions: the structure and kinematics of the milky way. The Astrophysical Journal **783**, 130 (2014).

[84] Anderson, L., Bania, T., Balser, D. S. & Rood, R. T. The green bank telescope h ii region discovery survey. iii. kinematic distances. The Astrophysical Journal **754**, 62 (2012).

[85] Ramón-Fox, F. & Bonnell, I. A. Streaming motions and kinematic distances to molecular clouds. Monthly Notices of the Royal Astronomical Society **474**, 2028–2038 (2018).

[86] Baba, J. et al. The origin of large peculiar motions of star-forming regions and spiral structures of our galaxy. The Astrophysical Journal **706**, 471 (2009).

[87] Xu, Y., Reid, M., Zheng, X. & Menten, K. The distance to the perseus spiral arm in the milky way. Science **311**, 54–57 (2006).